ARTICLE OPEN ACCESS

New BBB Model Reveals That IL-6 Blockade Suppressed the BBB Disorder, Preventing Onset of NMOSD

Yukio Takeshita, MD, PhD,* Susumu Fujikawa, MD,* Kenichi Serizawa, PhD, Miwako Fujisawa, MD, Kinya Matsuo, MD, Joe Nemoto, MD, Fumitaka Shimizu, MD, PhD, Yasuteru Sano, MD, PhD, Haruna Tomizawa-Shinohara, PhD, Shota Miyake, Richard M. Ransohoff, MD, PhD, and Takashi Kanda, MD, PhD

Correspondence
Dr. Kanda
tkanda@yamaguchi-u.ac.jp

Neurol Neuroimmunol Neuroinflamm 2021;8:e1076. doi:10.1212/NXI.0000000000001076

Abstract

Background and Objectives

To evaluate the pathophysiology of neuromyelitis optica spectrum disorder (NMOSD) and the therapeutic mechanism and levels of interleukin-6 (IL-6) blockade (satralizumab), especially with respect to blood-brain barrier (BBB) disruption with the new in vitro and ex vivo human BBB models and in vivo model.

Methods

We constructed new static in vitro and flow-based ex vivo models for evaluating continued barrier function, leukocyte transmigration, and intracerebral transferability of neuromyelitis optica-immunoglobulin G (NMO-IgG) and satralizumab across the BBB using the newly established triple coculture system that are specialized to closely mimic endothelial cell contact of pericytes and endfeet of astrocytes. In the in vivo study, we assessed the effects of an anti–IL-6 receptor antibody for mice (MR16-1) on in vivo BBB disruption in mice with experimental autoimmune encephalomyelitis in which IL-6 concentration in the spinal cord dramatically increases.

Results

In vitro and ex vivo experiments demonstrated that NMO-IgG increased intracerebral transferability of satralizumab and NMO-IgG and that satralizumab suppressed the NMO-IgG–induced transmigration of T cells and barrier dysfunction. In the in vivo study, the blockade of IL-6 signaling suppressed the migration of T cells into the spinal cord and prevented the increased BBB permeability.

Discussion

These results suggest that (1) our triple-cultured in vitro and in ex vivo BBB models are ideal for evaluating barrier function, leukocyte transmigration, and intracerebral transferability; (2) NMO-IgG increased the intracerebral transferability of NMO-IgG via decreasing barrier function and induced secretion of IL-6 from astrocytes causing more dysfunction of the barrier and disrupting controlled cellular infiltration; and (3) satralizumab, which can pass through the BBB in the presence of NMO-IgG, suppresses the BBB dysfunction and the infiltration of inflammatory cells, leading to prevention of onset of NMOSD.

*These authors contributed equally to this work.

From the Department of Neurology and Clinical Neuroscience (Y.T., S.F., M.F., K.M., J.N., F.S., Y.S., T.K.), Yamaguchi University Graduate School of Medicine; Kenichi Serizawa (K.S., H.T.-S., S.M.), Haruna Tomizawa-Shinohara and Shota Miyake, Product Research Department, Chugai Pharmaceutical Co., Ltd, Kanagawa, Japan; and Richard M Ransohoff (R.M.R.), Third Rock Ventures, Boston, MA.

Go to Neurology.org/N for full disclosures. Funding information and disclosures deemed relevant by the authors, if any, are provided at the end of the article.

The Article Processing Charge was funded by the authors.

Glossary

AQP4 = aquaporin-4; **BBB** = blood-brain barrier; **EAE** = experimental autoimmune encephalomyelitis; **EC** = endothelial cell; **ELISA** = enzyme-linked immunosorbent assay; **hAST** = human astrocyte; **hEC** = human brain microvascular EC; **hPCT** = human pericyte; **IgG** = immunoglobulin G; **IL-6** = interleukin-6; **NF-κB** = nuclear factor-kappa B; **NMO-IgG** = neuromyelitis optica-immunoglobulin G; **NMOSD** = neuromyelitis optica spectrum disorder; **PBMC** = peripheral blood mononuclear cell; **SEM** = standard error of mean; **TEER** = transepithelial electrical resistance.

Neuromyelitis optica spectrum disorder (NMOSD) is an inflammatory disease of the CNS associated with recurrent optic neuritis and longitudinally extensive transverse myelitis.[1,2] A major characteristic of NMOSD is the development of antibodies against the water channel aquaporin-4 (AQP4), which is expressed mainly in astrocytic foot processes.[3,4] The immunoglobulin G (IgG) plasma fraction of patients with NMOSD (neuromyelitis optica-immunoglobulin G [NMO-IgG]) contains anti-AQP4 antibodies, leading to cellular cytotoxicity of astrocytes.[5-7] In order for peripherally produced anti-AQP4 antibodies to gain access to their target in the CNS, they need to penetrate the blood-brain barrier (BBB).[8] Accordingly, disruption of the BBB—which allows influx of humoral factors including autoantibodies through the dysfunctional barrier and infiltration of inflammatory cells—is considered to be the first key step in the pathogenesis of NMOSD.[9-11] In fact, the ratio of CSF to serum albumin (CSF:serum albumin ratio), which is a marker of BBB permeability, is correlated with the clinical severity of NMOSD.[12,13]

Levels of interleukin-6 (IL-6) are elevated in the CSF and serum of patients with NMOSD compared with levels in patients with MS or noninflammatory neurologic disease.[14-16] There are various hypotheses in NMOSD pathophysiology, and IL-6 could promote the plasmablast survival and the production of antibodies against AQP4[17] in NMOSD. Then, in earlier studies,[11,18] we found that NMO-IgG induced IL-6 in astrocytes, which could decrease barrier function and increase the leukocyte transmigration, by attacking AQP4 of astrocytes using human astrocyte (hAST) cell lines with or without AQP4 and that anti-GRP78 and anti-AQP4 autoantibodies in NMO-IgG were important factors in the breakdown of the BBB via induction of IL-6 expression in astrocytes. In recent ex vivo experiments, inhibition of IL-6 signaling was shown to inactivate the effector functions of plasmablasts, which are a major source of NMO-IgG in the peripheral blood.[17] With respect to BBB disruption, IL-6 reduces the expression of endothelial tight junction proteins in a dose-and time-dependent manner and increases the permeability of human brain microvascular endothelial cells (hECs).[19] In patients with NMOSD, increased IL-6 in the CSF is correlated with the CSF: serum albumin ratio.[20] Overall, these reports suggest that IL-6 signaling pathways are involved in the pathogenesis of NMOSD. In fact, clinical research has demonstrated that treatment with anti-IL-6 receptor antibody ameliorates the disease in patients with NMOSD.[21,22]

Satralizumab is a humanized immunoglobulin G subclass 2 monoclonal antibody against IL-6 receptors; it specifically binds to both membrane-bound and soluble forms of IL-6 receptors and blockades IL-6 signaling pathways.[23] The constant and variable regions of satralizumab are engineered to have pH-dependent binding to IL-6 receptors, increased affinity to the neonatal Fc receptor, and a lower isoelectric point to extend the elimination half-life of the drug in plasma.[24,25] Importantly, it is reported that satralizumab showed beneficial effects such as a lower risk of relapse than with placebo among patients with NMOSD in an international, randomized, double-blind, placebo-controlled, phase 3 trial.[26] However, the therapeutic mechanisms of satralizumab, especially those with respect to BBB disruption, still remain unknown because there are no ideal in vitro BBB models with which to explore NMOSD pathogenesis.

To address this pertinent issue, we propose some important properties that will be necessary for an in vitro BBB model that is more robust than those currently available.[27] To construct in vitro BBB models with these properties, we used hECs (TY10), hASTs with AQP4 expression, and human pericytes (hPCTs), each of which was conditionally immortalized by transfection with temperature-sensitive SV40 (simian virus 40) large T antigen (ts-SV40-LT) and which retains both their physiologic and morphologic BBB properties.[28,29,33,34] We earlier constructed flow-based ex vivo models of hECs cocultured with hASTs that enable us to evaluate the transmigration of leukocytes across the endothelium under shear forces.[11,30,31] However, there were no ideal triple cocultured in vitro and ex vivo BBB model in which pericytes and the endfeet of astrocytes can directly contact endothelial cells (ECs). Then, it was impossible to evaluate the barrier function, leukocyte transmigration, and intracerebral transferability to reveal NMOSD pathogenesis.

In the present study, we constructed functional in vitro static and ex vivo flow-based models using the newly established triple coculture system. The new static in vitro model allowed long-term measurement of transepithelial electrical resistance (TEER) and measurement of microvolumes of IgG translocation through the BBB. The new ex vivo flow-based model enabled us to evaluate leukocyte transmigration across the BBB. Then, we evaluated the effects of satralizumab on BBB disruption caused by NMO-IgG. We also assessed the effects of an anti–IL-6 receptor antibody for mice (MR16-1) on in vivo BBB disruption in mice with experimental autoimmune encephalomyelitis (EAE). These mice are used as an animal model of CNS autoimmune diseases in which IL-6 concentration in the spinal cord dramatically increases.[32]

Methods

Human Subjects

The Institutional Review Boards of Yamaguchi University Graduate School of Medicine and Chugai Pharmaceutical Co., Ltd, approved all study protocols, and signed informed consent was obtained from each blood donor.

NMO-IgG, Control IgG, and Satralizumab

NMO-IgG was the IgG fraction isolated from pooled serum collected from 10 patients with NMOSD, and control IgG isolated from pooled serum collected from healthy volunteers at the Yamaguchi University Graduate School of Medicine. Both NMO-IgG and control IgG were purified by protein G affinity and adjusted for assays by extensive dialysis. Anti-AQP4 and anti-GRP78 antibodies were previously detected in NMO-IgG but not in control IgG. Satralizumab was prepared at Chugai Pharmaceutical Co., Ltd. We used NMO-IgG, control IgG, and satralizumab at a final concentration of 100 μg/mL.

Cell Culture

hECs used were adult human brain microvascular ECs transfected. hECs, hAST and hPCT and immortalized with a plasmid encoding ts-SV40-LT as previously described.[28,29,33,34] hECs and hASTs were cultured as previously described.[30] hPCTs were maintained in Dulbecco's Modified Eagle's Medium (Gibco BRL) supplemented with 10% (v/v) heat-inactivated fetal bovine serum and antibiotics (100 UI/mL penicillin G sodium, 100 μg/mL streptomycin sulfate). Astrocyte medium was used as the coculture medium.

Triple Coculture System

hPCTs and hASTs were cocultured on Transwell insert membranes having 3-μm pores (Corning Life Sciences, Tewksbury, MA), with hPCTs on the luminal side and hASTs on the abluminal side. hECs were cultured in Nunc dishes with an UpCell surface (Thermo Fisher Scientific, Waltham, MA), which afford sheet-like detachment of confluent cells and extracellular matrix when the temperature is shifted to 20°C. The sheet of confluent hECs was detached and transferred onto the hPCTs cocultured with hASTs on the insert. The polymers of the UpCell surface are slightly hydrophobic at 37°C but become hydrophilic at 20°C to form an aqueous film between cells and polymers resulting in sheet-like detachment of cells including their surrounding native extracellular matrix structures.

Real-Time Monitoring System for TEER Measurements With cellZscope

The triple cocultured inserts were transferred to an automated cell monitoring system (cellZscope; CellSeed Inc., Tokyo, Japan). After addition of satralizumab and NMO-IgG or control IgG to the vascular (hEC) side or the brain parenchymal (hAST) side or to both sides, the TEER values were measured using the cellZscope device, which can record the TEER every minute for 96 hours.

Transmigration Assay

The isolation of peripheral blood mononuclear cells (PBMCs) and flow-based transmigration assays were performed in a 3D BioFlux flow chamber device (Fluxion Bioscience, San Diego, CA) as previously described.[30] The migrated cells were enumerated by a hemocytometer and then normalized to migrated cell numbers determined by flow cytometry. After collection, cells were fixed for 10 minutes in 1% paraformaldehyde at room temperature and washed in phosphate buffered saline + 0.1 mM ethylenediaminetetraacetic acid, followed by blocking in mouse IgG. Cells were labeled with anti-human CD45 eFluor450, CD8a APC-eFluor780 (eBioscience, San Diego, CA), CD3A-lexa Fluor 647 (BioLegend, San Diego, CA), CD19 BV711, and CD4 PE-CF594 (BD Biosciences). Data were acquired using BD FACSCanto II (BD Biosciences) and analyzed by FlowJo software (v.10.4.1; Treestar, Ashland, OR).

Measurement of Microvolume IgG Translocation by Odyssey Infrared Imaging System

Control IgG and satralizumab were labeled with IRDye 800CW protein (IRDye 800CW Protein Labeling Kit; LI-COR, Lincoln, NE) following the manufacturer's protocol. After exposing hECs in triple cocultured inserts to labeled control IgG or satralizumab, the microvolumes that translocated to the lower chamber were detected by an Odyssey Infrared Imaging System (LI-COR), and the apparent BBB permeability coefficient (Papp; mm/seconds) was calculated as previously described.[30]

Measurement of Microvolume IgG Translocation by a Spectrophotometer

NMO-IgG or control IgG was added to hECs in triple cocultured inserts and incubated for 12 hours. Following the manual of the Easy-Titer Antibody Assay Kit (Thermo), anti-human IgG coated beads were added to the lower well and incubated with the sample for 60 minutes. Accumulated IgG in the lower well was measured by a spectrophotometer, following the manufacturer's instructions. The total amount of accumulated IgG was normalized to 1 using control IgG and reported as IgG accumulation.

Measurement of Microvolume Satralizumab Translocation by Enzyme-Linked Immunosorbent Assay

After exposing hECs in triple cocultured inserts to satralizumab plus NMO-IgG or satralizumab plus control IgG for 24 hours, the concentration of satralizumab in the lower chamber was measured by using enzyme-linked immunosorbent assay (ELISA) with anti-satralizumab antibody. The samples were run according to the manufacture's protocol. The total amount of accumulated satralizumab was normalized to 1 using control IgG + satralizumab and reported as satralizumab accumulation.

Experimental Design of EAE Mice

Female C57BL/6J mice (7 weeks old; Charles River Laboratories Japan, Inc., Kanagawa, Japan) were used. EAE was

Figure 1 Construction of Newly In Vitro BBB Model With Triple Coculture System of Temperature-Sensitive Conditionally Immortalized Human BBB Cell Lines

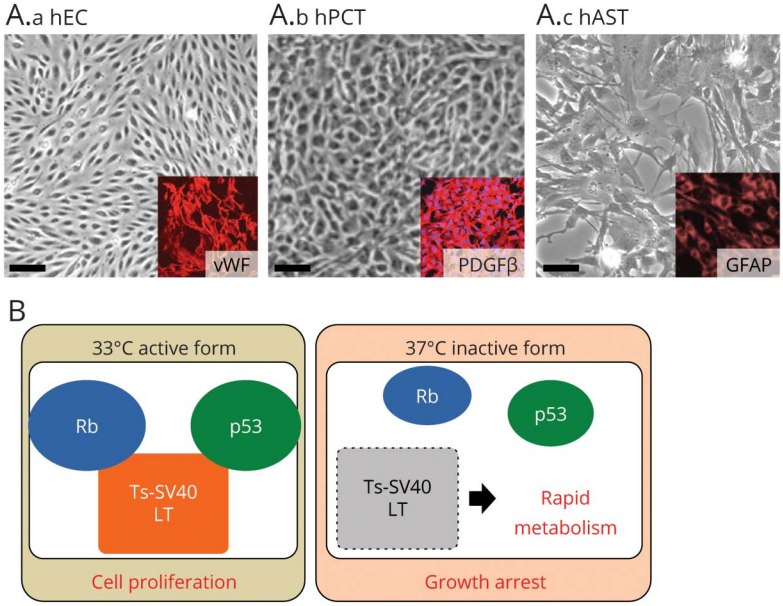

(A) Establishment of the BBB cell lines that maintain the BBB properties. Morphology of hEC is spindle-shape. hEC expressed von Willebrand factor (vWF) as a lineage marker of endothelium. Morphology of hPCT is cobblestone-shape. hPCT expressed PDGFß as a lineage marker of pericyte. Morphology of hAST is star-shape. hAST expressed glial fibrillary acidic protein (GFAP) as a lineage marker of hAST. (B) Three conditionally immortalized human cell lines were transfected with temperature-sensitive SV40 large T antigen (Ts-SV40 LT). At 33°C, activated Ts-SV40 LT binds and inhibits p53 and Rb, which are strong tumor suppressors, leading to continuous cell proliferation. At 37°C, inactivated Ts-SV40 LT exhibits growth arrest, leading to differentiation into mature cells. BBB = blood-brain barrier; hAST = human astrocyte; hEC = human brain microvascular EC; hPCT = human pericyte.

induced in mice by subcutaneous immunization (on day 0) with 50 μg of the myelin oligodendrocyte glycoprotein 35–55 peptide (MOG35-55; Peptide International, Louisville, KY) emulsified in complete Freund adjuvant (Difco Laboratories, Detroit, MI) supplemented with *Mycobacterium tuberculosis* extract H37Ra (Difco Laboratories). In addition, mice received 250 ng pertussis toxin (List Biological Laboratories, Campbell, CA) IV on day 0 and intraperitoneally on day 2. Control mice were treated with complete Freund adjuvant and saline alone. Anti-IL-6 receptor antibody (MR16-1) was prepared using a hybridoma established in Chugai Pharmaceutical's laboratories.[38] The EAE mice were intraperitoneally administered MR16-1 (8 mg/mouse) on day 7 after MOG35-55 immunization. On day 15 or 16 after MOG35-55 immunization, spinal cords, spleens, and sera were harvested for immunohistochemistry, flow cytometry, and TEER studies. EAE mice were sequentially scored for clinical signs of EAE according to the following scale: 0, no apparent disease; 1, limp tail; 2, hind limb weakness; 3, hind limb paresis; 4, hind limb paralysis; 5, hind limb and forelimb paralysis; and 6, moribundity and death.

Immunohistochemistry

Mice were anesthetized with isoflurane, and transcardial perfusion was performed with 20 mL of cold phosphate buffered saline. The L3–L5 segment of the lumbar spinal cord was removed, fixed in 4% paraformaldehyde, and placed in a 30% sucrose solution overnight. Samples were embedded in optimal cutting temperature compound, and frozen slices of spinal cord (10 μm thick) were obtained with a cryostat. Spinal cord slices were stained by using the following primary antibodies: goat anti-albumin antibody (1:200, A90-134A; Bethyl Laboratories, Inc., Montgomery, TX), biotin-conjugated donkey anti-mouse IgG antibody (1:200, 715-066-151; Jackson ImmunoResearch, West Grove, PA), and rat anti-CD4 antibody (1:100, 550280; BD Pharmingen Inc., San Diego, CA). After overnight incubation with primary antibodies at 4°C, spinal cord sections were incubated with secondary antibody Alexa Fluor 488-conjugated donkey anti-goat IgG (1:200, 705-546-147; Jackson ImmunoResearch) and Alexa Fluor 488-conjugated streptavidin (2 μg/mL, 016-540-084; Jackson ImmunoResearch). For CD4 staining, biotin-conjugated donkey anti-rat IgG (1:200, 712-066-153; Jackson ImmunoResearch) and Alexa Fluor 488-conjugated streptavidin (2 μg/mL, 016-540-084; Jackson ImmunoResearch) were used. Slides were mounted using Vectashield Antifade Mounting Medium (H-1200; Vector Laboratories, Burlingame, CA). Spinal cord slices were randomly selected from each mouse and observed under a BZ-9000 Fluorescence Microscope (Keyence, Osaka, Japan). Positive staining areas were calculated using the BZ-II analyzer (Keyence), and CD4-positive T cells were counted with imaging analysis software (WinROOF Version 6.3.1; Mitani Corporation, Fukui, Japan).

Flow Cytometry In Vivo Study

Spleens collected from control mice and EAE mice were homogenized and passed through a 100- and 40-μm cell strainer to isolate mononuclear cells. Red blood cells were hemolyzed with ammonium-chloride-potassium lysing buffer (Gibco, Carlsbad, CA). Mononuclear cells were incubated with Mouse BD Fc Block (BD Pharmingen Inc.) before staining. The cells were initially stained with fluorescein isothiocyanate-conjugated anti-CD4 antibody (100510; BioLegend) and then intracellularly stained using PE-conjugated anti-IL-17A (506904; BioLegend)

Figure 2 Construction of Ex Vivo BBB Model With Triple Coculture System for Leukocyte Transmigration and Effect of Satralizumab on NMO-IgG–Induced Transmigration of Leukocytes in Ex Vivo

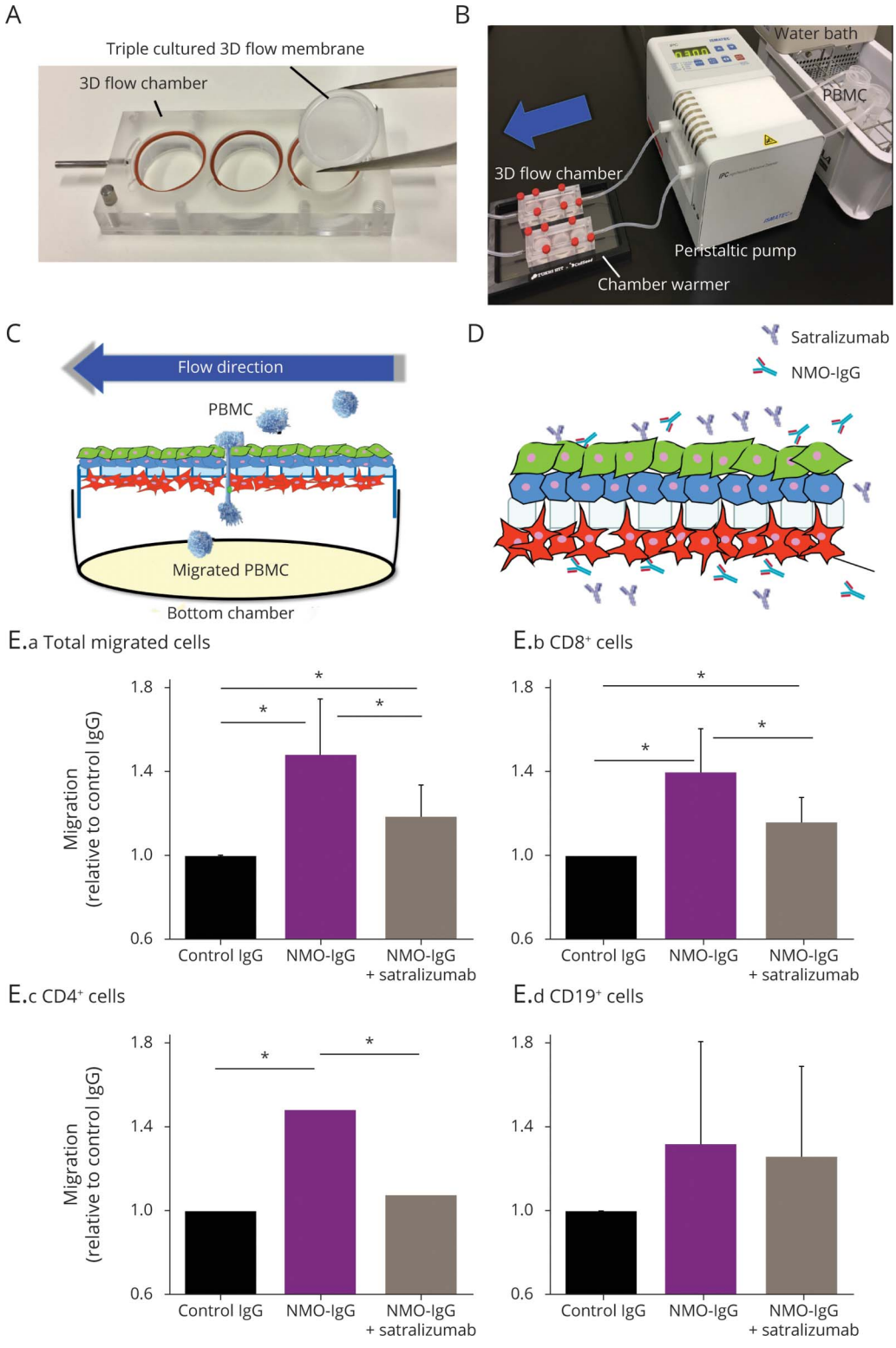

(A) 3D flow chamber and 3D flow membrane. The triple-cultured membranes were transferred in a 3D chamber. (B) Whole setup of migration assay under shear forces. Normal human PBMCs flowed onto luminal side with physiologic shear force by peristaltic pomp. (C) Schema of the 3D flow chamber in transmigration assay. Total migrated cells were recovered from the bottom chamber and enumerated. (D) Schema of leukocyte transmigration assay with NMO-IgG and/or satralizumab. (E) Flow-based leukocyte transmigration assays using a 3D flow chamber showed that application of NMO-IgG increased the numbers of total migrating PBMCs and $CD4^+$, $CD8^+$, and $CD19^+$ cells relative to numbers migrating with control IgG and that the application of NMO-IgG plus satralizumab significantly suppressed that increase. *$p < 0.05$ by unpaired t test (n = 6 per group). All data are expressed as mean and standard error of mean. PBMC = peripheral blood mononuclear cells.

Figure 3 Effects of IL-6 Receptor Blockade on Lymphocyte Migration Into the Spinal Cord In Vivo

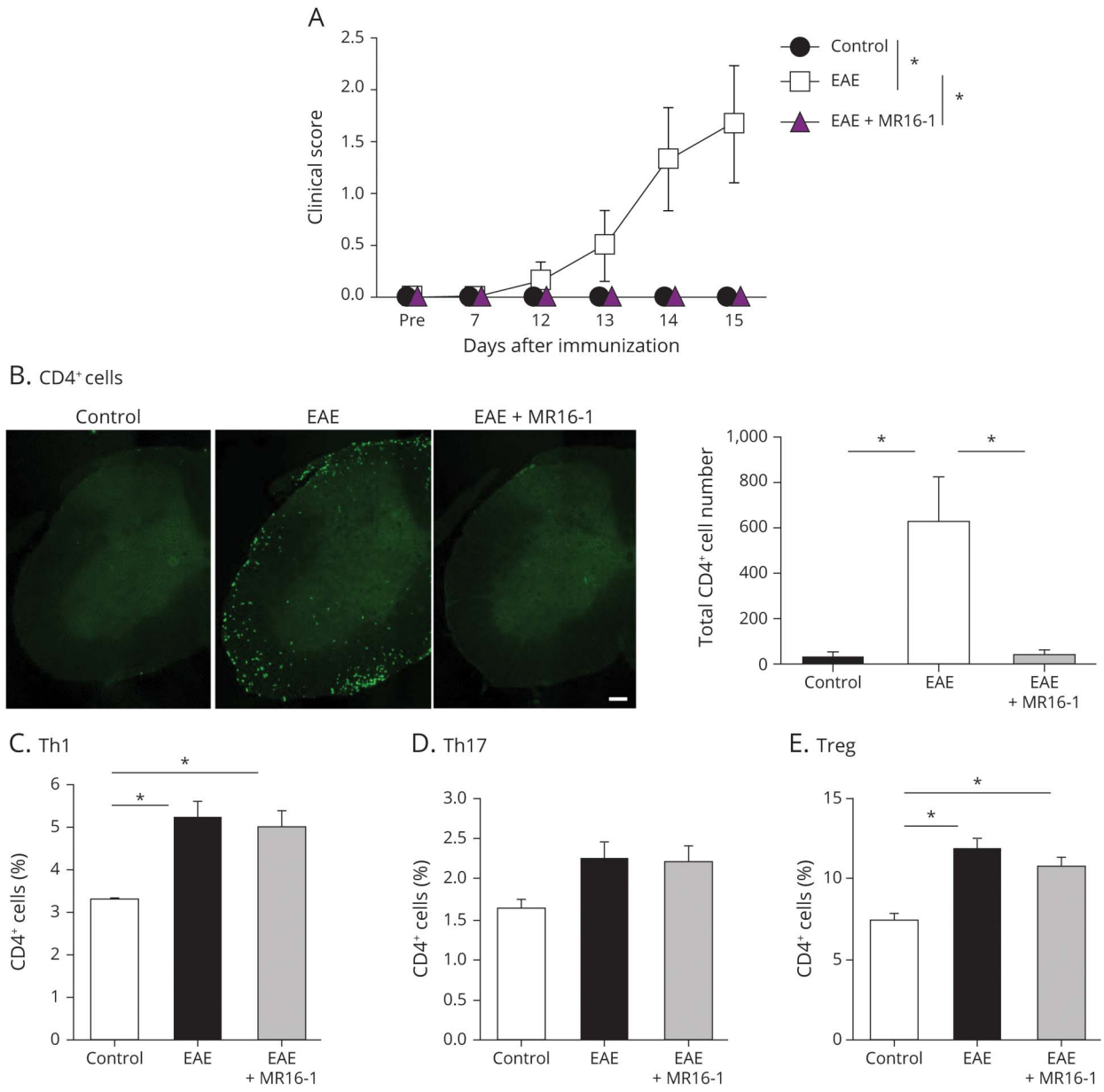

(A) Anti–IL-6 receptor antibody (MR16-1) was administered on day 7 after immunization. Anti–IL-6 receptor antibody significantly prevented the onset of clinical signs in EAE mice. *$p < 0.05$ by 2-way analysis of variance (n = 3–6 per group). (B) Anti–IL-6 receptor antibody suppressed lymphocyte migration into the spinal cords of EAE mice. Representative images showing immunohistochemical staining for $CD4^+$ cells in the spinal cord on day 15 after immunization. The number of $CD4^+$ T cells was markedly increased in the spinal cord of EAE mice. Anti–IL-6 receptor antibody administered on day 7 after immunization significantly prevented this increase. *$p < 0.05$ by Tukey multiple comparison test (n = 3–6 per group). Scale bar = 100 μm. (C) The induction of Th1 cells and (E) FoxP3-positive regulatory T cells was significantly upregulated on day 16 after immunization. There was a tendency, but not significantly, for Th17 cells to increase in EAE mice (D). Administration of anti–IL-6 receptor antibody on day 7 after immunization did not change the induction of these in EAE mice. *$p <$ 0.05 by Tukey multiple comparison test (n = 4–8 per group). All data are expressed as mean and standard error of mean. EAE = experimental autoimmune encephalomyelitis; IL-6 = interleukin-6.

and APC-conjugated anti-interferon-γ (505810; BioLegend) antibodies; staining was performed with the Fixation/Permeabilization Solution Kit with BD GolgiPlug (BD Biosciences) according to the manufacturer's protocol. For analysis of Treg cells, Fc-blocked cells were initially stained with fluorescein isothiocyanate-conjugated anti-CD4 and BV421-conjugated anti-CD25 (102034; BioLegend) antibodies and then intracellularly stained using the APC-conjugated anti-Foxp3 antibody (17-5773-80B; Invitrogen, Carlsbad, CA); staining was performed with a Foxp3 Transcription Factor Staining Buffer Set (Invitrogen) according to the manufacturer's protocol. Data were acquired using BD FACSCanto II (BD Biosciences) and analyzed using FlowJo 10.4.1 (Treestar).

Statistical Analysis

All data are expressed as mean and standard error of mean (SEM). The statistical significance of differences was determined by using the unpaired *t* test, Tukey multiple

Figure 4 Effects of IL-6 Receptor Blockade on BBB Permeability In Vivo

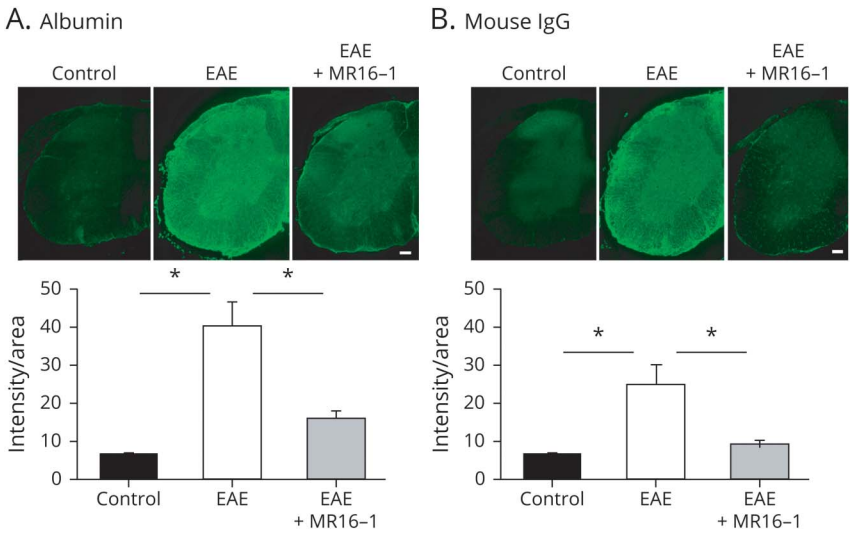

(A and B) Representative images showing immunohistochemical staining for albumin (A) and IgG (B) in the spinal cord on day 15 after immunization. Leakage of albumin and IgG into the spinal cord was higher in EAE mice than in control mice and was significantly reduced by treatment with anti–IL-6 receptor antibody (MR16-1). *$p < 0.05$ by Tukey multiple comparison test (n = 3–6 per group). Scale bars = 100 μm. All data are expressed as mean and standard error of mean. EAE = experimental autoimmune encephalomyelitis.

comparison test with analysis of variance, or 2-way analysis of variance for comparison of time course data. Probability values of less than 0.05 were considered significant. Statistical analyses were performed using IBM SPSS Statistics (International Business Machines Corporation, Armonk, NY) or JMP version 11.2.1 software (SAS Institute, Cary, NC).

Results

Construction of Newly In Vitro BBB Models

We used human brain microvascular ECs (hECs; TY10), hASTs with AQP4 expression, and hPCTs, each of which was conditionally immortalized by transfection with ts-SV40-LT (Figure 1A). These transfected cell lines proliferate at 33°C due to ts-SV40 LT's temperature sensitive inhibition activity of p53 and Rb. On the other hand, cells could differentiate into mature cells at 37°C because Ts-SV40 LT is inactivated and exhibit growth arrest[28,33,34] (Figure 1B). In these previous articles, we confirmed the expression markers of hECs, hASTs, and hPCTs (hECs; occludin, Claudin-5, Claudin-12, ZO-1, ZO-2, JAM-A, GLUT-1, CAT-1, LAT-1, 4F2hc, MCT-1, calreticulin, MDR1, ABCG2, MRP1, MRP2, MRP4, and MRP5, and hASTs; glial fibrillary acidic protein, EAAT2, and AQP4, hPCTs; platelet-derived growth factor receptor beta, Desmin, Kir 6.1, osteopontin, alfa smooth muscle actin, and NG2). To construct triple coculture systems of these human BBB cell lines, multiple steps were organized by including cell culture on Upcell dish with coated temperature-responsive polymer (eFigure 1, A and B, links.lww.com/NXI/A591). First, hASTs were cultured on abluminal side of insert membranes having 3-μm pores and incubated for 24 hours so that some astrocytic endfeet with AQP4 could protrude through the membrane pores (eFigure 1C and links.lww.com/NXI/A591). Second, after culturing of hPCTs on the luminal side of membranes (eFigure 1E, links.lww.com/NXI/A591), hASTs and hPCTs were cocultured at 33°C for 24 hours. Third, hECs were cultured on Upcell dish with coated temperature-responsive polymer, which can achieve sheet-like detachment of confluent cells and extracellular matrix by temperature shifting to 20°C (eFigure 1, F and *G*, links.lww.com/NXI/A591). Then, sheet-like detachment of confluent hECs was transferred onto the hPCTs. After cocultuting of these cell lines at 33°C for 24 hours, they differentiated into mature cells under the condition of 37°C. Confocal 3D analysis with living staining of each cell line showed that multicultured insert constituted the five-layer structures, which is consisted of hECs, hPCTs, astrocytic endfeet, membrane, and hAST (eFigure 1, H, links.lww.com/NXI/A591). Some endfeets protruded through the membrane pores. hPCTs and endfeet of hASTs were close to the hEC layer.

Construction of Ex Vivo BBB Model and Effect of Satralizumab on NMO-IgG–Induced Transmigration of Leukocytes

To evaluate the effect of satralizumab on NMO-IgG–induced transmigration of leukocytes, we constructed a flow-based dynamic BBB model incorporating hEC/hPCT/hAST triple coculture, which allows further investigation of leukocyte transmigration under flow (Figure 2, A–C). After exposing the EC side (vascular side) and the astrocyte side (brain parenchymal side) to satralizumab plus NMO-IgG or to NMO-IgG alone (Figure 2D), we counted the total numbers of all migrating cells and the numbers of phenotyped cells and compared their migrations relative to those with control IgG. Application of NMO-IgG increased the migrations of all PBMCs and $CD4^+$, $CD8^+$, and $CD19^+$ cells relative to their migrations with control IgG, and the application of NMO-IgG plus satralizumab significantly suppressed this increase in the relative numbers of migrating PBMCs and $CD4^+$ and $CD8^+$ cells (Figure 2E).

Figure 5 Effects of Satralizumab on the Barrier Function of the BBB In Vitro

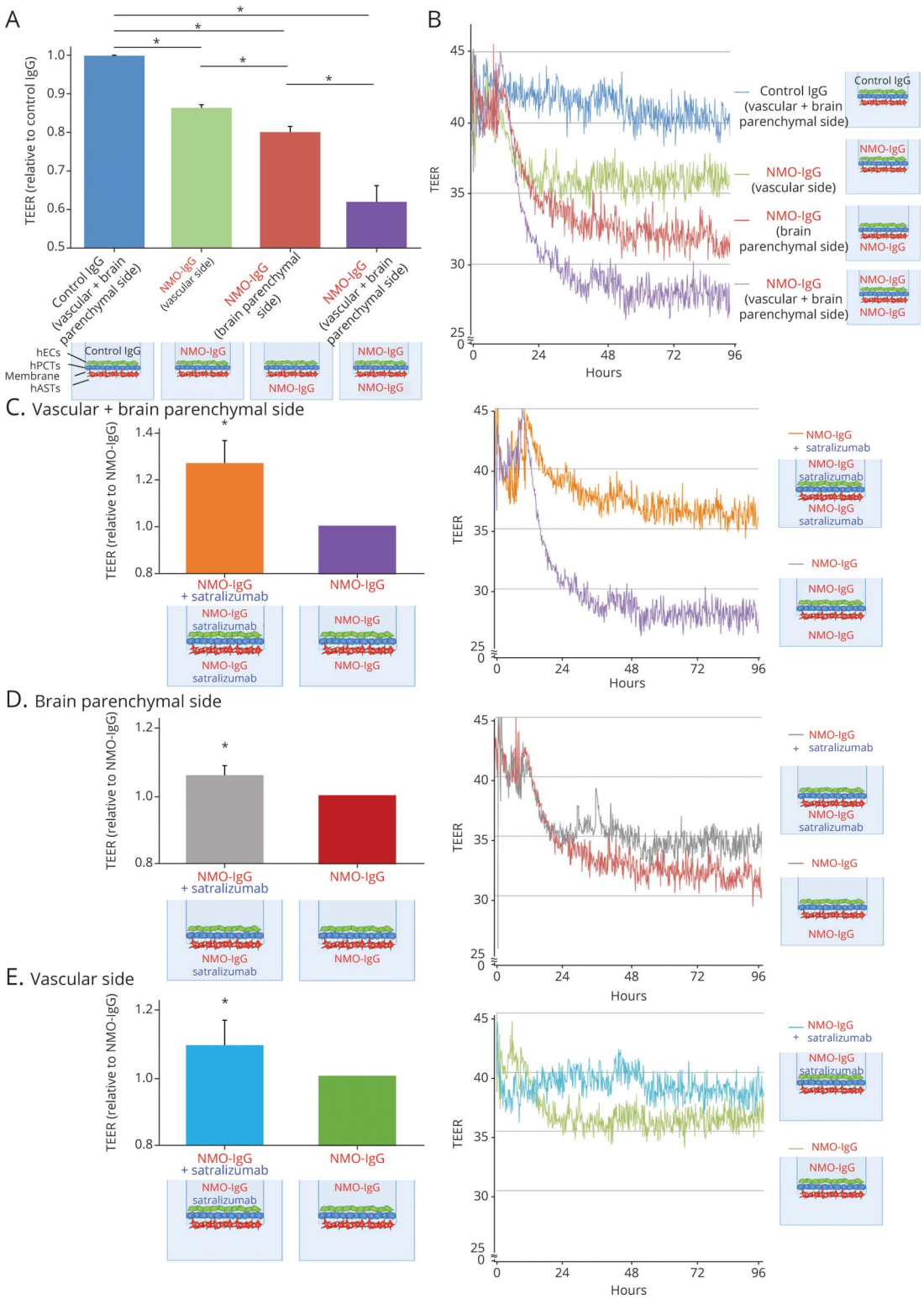

(A) Application of NMO-IgG to either the vascular side or the brain parenchymal side or both sides of the static BBB model significantly decreased the TEER value relative to that of control IgG at 72 hours. *$p < 0.05$ by unpaired t test (n = 3 per group). (B) Real-time TEER measurement by cellZscope showed that the TEER values had started to decrease within 24 hours of application of NMO-IgG in all groups, and the declining trend continued for 48 hours. (C–E, left panels) After addition of satralizumab and NMO-IgG to either the vascular side or the brain parenchymal side or both sides, the TEER values under conditions of satralizumab plus NMO-IgG were significantly higher than under conditions of NMO-IgG alone at 72 hours. *$p < 0.05$ by unpaired t test (n = 3 per group). All data are expressed as mean and standard error of mean. (C–E, right panels) Real-time TEER measurement by cellZscope showed a declining trend in TEER values under conditions of satralizumab plus NMO-IgG in all groups, but the decline remained less than that for NMO-IgG alone for 96 hours.

Figure 6 Intracerebral Transferability of Satralizumab in the Presence of NMO-IgG In Vitro

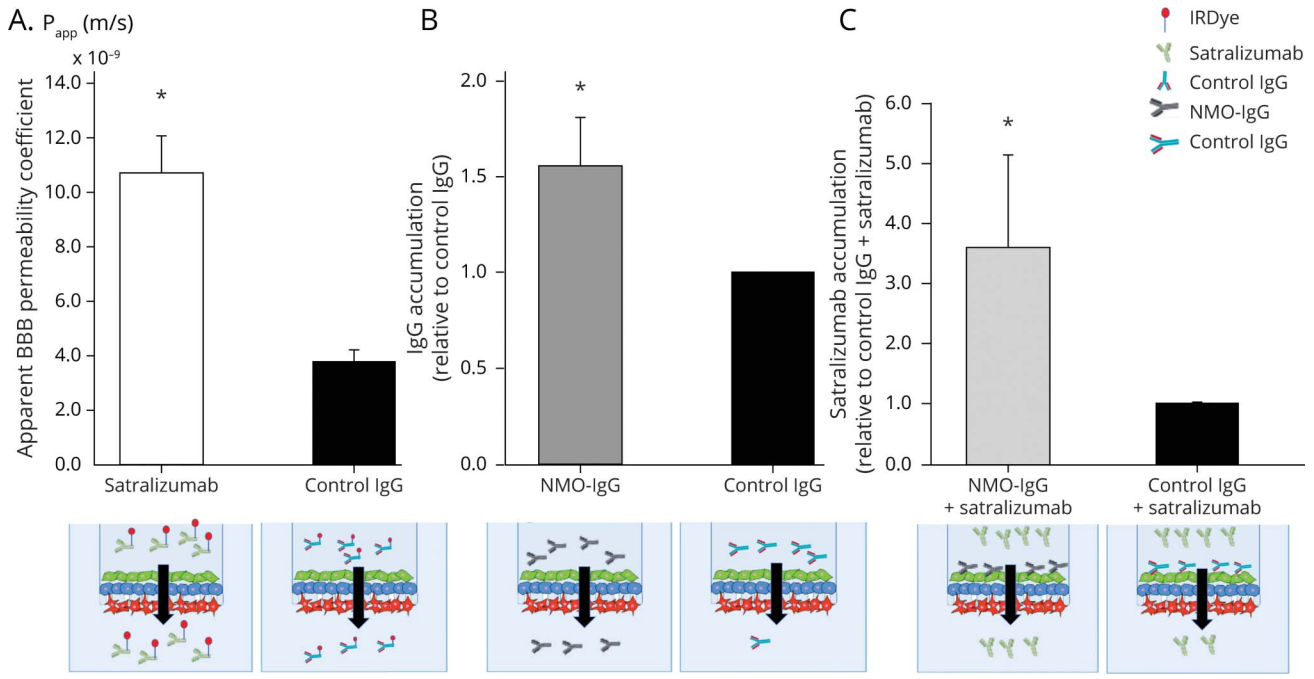

(A) Analysis of microvolume IgG translocation through the BBB by the Odyssey Infrared Imaging System revealed that the BBB Papp for satralizumab was almost 3 times that for control IgG. *$p < 0.05$ by unpaired *t* test (n = 6 per group). (B) Analysis of microvolume IgG translocation through the BBB by the spectrophotometer revealed that the relative accumulation of IgG for NMO-IgG was almost 1.5 times that for control IgG. *$p < 0.05$ by unpaired *t* test (n = 6 per group). (C) ELISA with anti-satralizumab antibody showed that the relative accumulation of satralizumab for satralizumab + NMO-IgG was significantly increased to almost 3 times that for satralizumab + control IgG. *$p < 0.05$ by unpaired *t* test (n = 8 per group). All data are expressed as mean and standard error of mean.

Effects of IL-6 Receptor Blockade in EAE Mice

Administration of MR16-1 (anti–IL-6 receptor antibody for mice) on day 7 after induction of EAE significantly and strongly prevented the onset of clinical signs in EAE mice (Figure 3A). We then confirmed the effect of MR16-1 on leukocyte transmigration in EAE mice. On day 15, the number of $CD4^+$ T cells markedly increased in the spinal cords of EAE mice, whereas these cells were almost undetected in the spinal cords of control mice (control, 33.7 ± 21.5 [mean ± SEM] cells/spinal cord slice; EAE, 628.3 ± 196.5 cells/spinal cord slice) (Figure 3B). Administration of MR16-1 on day 7 significantly prevented the migration of $CD4^+$ T cells into the spinal cord (EAE + MR16-1, 40.3 ± 17.7 cells/spinal cord slice) (Figure 3B). To exclude the possibility that the impact of MR16-1 on clinical signs and on leukocyte migration into the spinal cord was secondary to changes in the immune response, we evaluated the effect of MR16-1 on T-cell differentiation in EAE mice. In splenocytes, Th1 cells and FoxP3-positive regulatory T cells were significantly increased on day 16 in EAE mice (Figure 3, C and E). Th17 cells showed a tendency, but not significantly, to increase in EAE mice (Figure 3D). Administration of anti–IL-6 receptor antibody on day 7 did not affect the induction of these in EAE mice (Figure 3, C–E).

Effects of IL-6 Receptor Blockade on the Barrier Function in EAE Mice

Immunohistochemical analysis on day 15 showed that leakage of albumin and IgG into the spinal cord was higher in EAE mice than in control mice (Figure 4, A and B). This leakage into the CNS indicates the increased permeability of the BBB. Treatment of EAE mice with MR16-1 significantly prevented these leakages into the spinal cord. As regards the inhibiting effect on barrier dysfunction with application of satralizumab on the vascular side, we showed that sera from EAE mice mildly reduced the barrier function of ECs in monoculture (eFigure 2, links.lww.com/NXI/A592) Serum from EAE mice at onset of EAE on day 16 after immunization significantly decreased the TEER value of a monolayer of mouse primary BMECs. Anti–IL-6 receptor antibody significantly prevented this reduction.

Effects of Satralizumab on the Barrier Function In Vitro

To evaluate whether NMO-IgG affects the barrier function of the BBB on the vascular side or the brain parenchymal side, we constructed the static in vitro BBB model, which allowed long-term measurement of real-time TEER. After addition of NMO-IgG or control IgG with either the vascular side, the brain parenchymal side, or both sides, the TEER values were measured in every minute for 5 consecutive days. Within 24 hours of application of NMO-IgG, TEER values in all groups had begun to decrease compared with control IgG, and at 72 hours, they had significantly decreased in all groups (Figure 5, A and B). Application of NMO-IgG to both the vascular and brain parenchymal sides resulted in the lowest TEER values of all groups. TEER values with brain parenchymal application of NMO-IgG were significantly lower than TEER values with vascular application of NMO-IgG.

Figure 7 The Pathophysiology of NMOSD at the BBB and the Action Mechanism of Satralizumab at the BBB

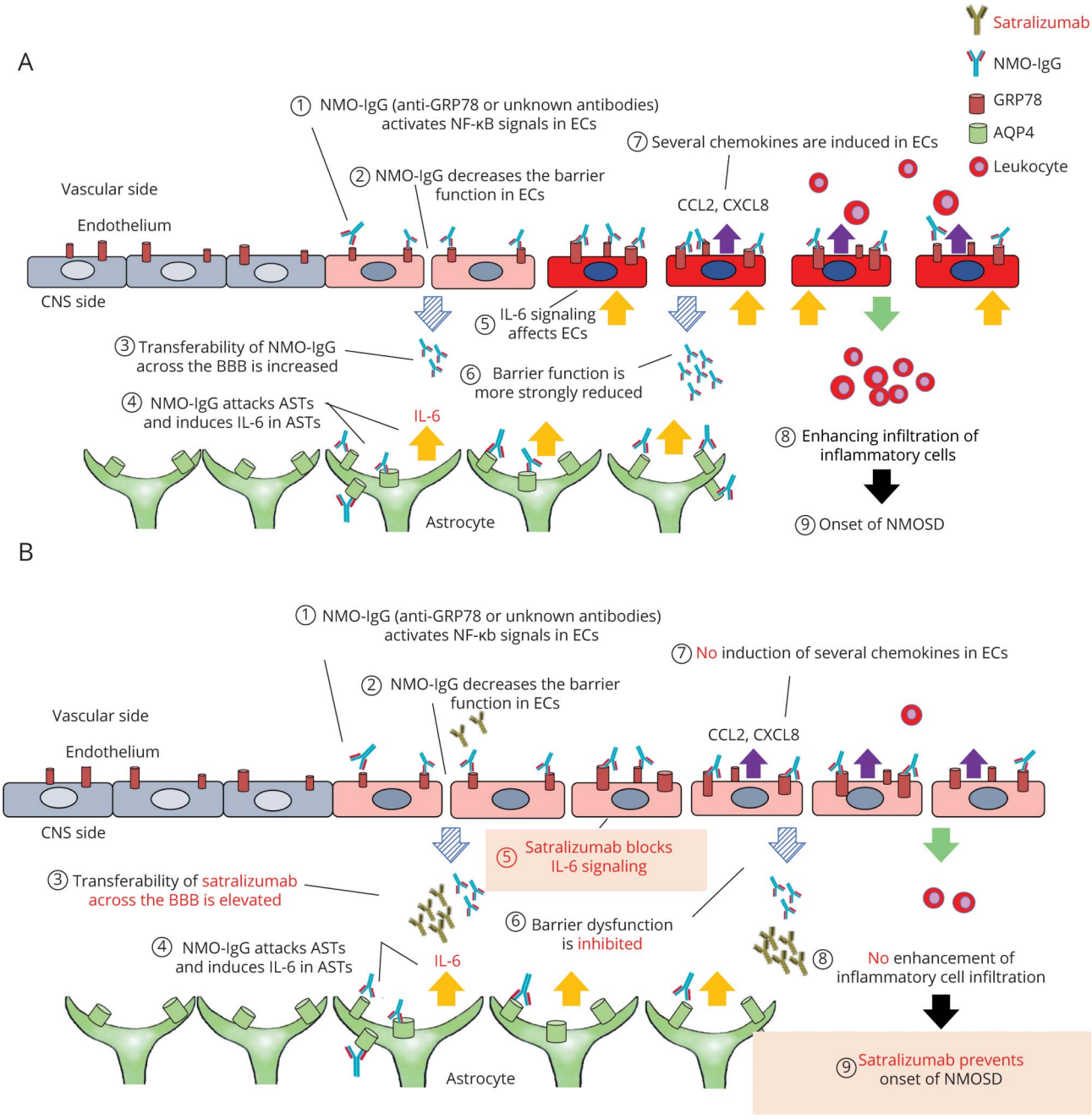

(A) There are several steps on both sides of the BBB involved in the onset of NMOSD. First, NMO-IgG (anti-GRP78 or an unknown antibody or antibodies) activates nuclear factor-kappa B (NF-κB) signals in ECs. Second, NMO-IgG decreases the barrier function on the vascular side. Third, NMO-IgG increases the intracerebral transferability of NMO-IgG itself. Fourth, NMO-IgG attacks the AQP4 of astrocytes (ASTs) and induces IL-6 expression in ASTs. Fifth, IL-6 signaling affects endothelial cells on the CNS side. Sixth, IL-6 signaling more strongly decreases the barrier function on the CNS side than on the vascular side. Seventh, IL-6 signaling induces the expression of several chemokines (CCL2 and CXCL8) in endothelial cells. Eight, the induced chemokines enhance infiltration of inflammatory cells. Finally, NMOSD develops. (B) First, NMO-IgG (anti-GRP78 or an unknown antibody or antibodies) activates NF-κB signals in endothelial cells. Second, NMO-IgG decreases the barrier function on the vascular side. Third, NMO-IgG elevates the intracerebral transferability of satralizumab more than NMO-IgG. Fourth, NMO-IgG attacks the AQP4 of ASTs and induces IL-6 expression in ASTs. Fifth, satralizumab blocks IL-6 signaling on the CNS side. Sixth, satralizumab inhibits the reduction in barrier function by blockade of IL-6 signaling. Seventh, blockade of IL-6 signaling by satralizumab suppresses the expression of several chemokines (CCL2 and CXCL8) in endothelial cells. Eight, satralizumab inhibits infiltration of inflammatory cells. Finally, satralizumab prevents the onset of NMOSD. AQP4 = aquaporin-4; BBB = blood-brain barrier; EC = endothelial cell; IL-6 = interleukin-6; NMOSD = neuromyelitis optica spectrum disorder.

To evaluate whether satralizumab affects the BBB dysfunction induced by NMO-IgG, we used the static BBB model incorporating hEC/hPCT/hAST triple coculture with either the vascular side or the brain parenchymal side or both sides exposed to NMO-IgG. After addition of satralizumab plus NMO-IgG or control IgG to either the vascular side or the brain parenchymal side or both sides at the same time, TEER values were measured as mentioned above. Ahead of these

experiments, we confirmed that satralizumab did not affect the barrier function (eFigure 3, links.lww.com/NXI/A593). TEER values at 72 hours were significantly higher under conditions where both the vascular side and the brain parenchymal side were exposed to satralizumab plus NMO-IgG than under conditions of NMO-IgG alone (Figure 5C). The inhibiting effect of satralizumab on barrier dysfunction was almost the same when satralizumab was applied to the brain parenchymal side as it was when applied to the vascular side (Figure 5, D and E). Application of satralizumab to both the vascular and brain parenchymal sides had the highest inhibiting effect on barrier dysfunction among the 3 conditions (Figure 5, C and E).

Intracerebral Transferability of Satralizumab in the Presence of NMO-IgG In Vitro

To compare the microvolume translocation of satralizumab and NMO-IgG across the BBB, we constructed the in vitro BBB models in which measurement of microvolumes of satralizumab and IgG translocation through the BBB could be detected by Odyssey Infrared Imaging System and ELISA. We evaluated the apparent permeability coefficients of the BBB (Papp; mm/seconds) with respect to satralizumab and control IgG. Labeled satralizumab or IgG2 (control IgG) was added to the hEC (vascular) side. Then, the IgG that was translocated to the brain parenchymal side was detected by an infrared imaging system, and the apparent BBB permeability coefficients for satralizumab and control IgG were calculated. The Papp with respect to satralizumab was almost 3 times the Papp with respect to control IgG (Figure 6A).

After exposing the vascular side to NMO-IgG or control IgG, the translocated IgG was detected by the human IgG detection ELISA kit. The total amounts of accumulated IgG for NMO-IgG and control IgG were calculated, normalized with respect to control IgG, and reported as IgG accumulation. The intracerebral transferability of NMO-IgG was almost 1.5 times that of control IgG (Figure 6B).

In a previous study, we found the transfer rate of MR16-1 across the BBB in EAE mice to be almost 30 times that of normal mice.[32] Thus, we explored whether the intracerebral transferability of satralizumab would be similarly increased in the presence of NMO-IgG. After exposing the vascular side of the triple coculture BBB model to satralizumab plus NMO-IgG or to satralizumab plus control IgG at the same time, the accumulated satralizumab was measured by ELISA with anti-satralizumab antibody. The total amount of satralizumab for NMO-IgG plus satralizumab was normalized with respect to control IgG plus satralizumab and reported as satralizumab accumulation. The relative satralizumab accumulation for NMO-IgG plus satralizumab was significantly increased to almost 3 times that for control IgG plus satralizumab (Figure 6C).

Discussion

We successfully generated in vitro and in ex vivo BBB models using the newly established triple coculture system of human BBB cell lines (Figure 1 and eFigure 1, links.lww.com/NXI/A591). In in vitro studies, application of satralizumab to the vascular and brain parenchymal sides of the model suppressed the transmigration of total PBMCs and $CD4^+$ and $CD8^+$ cells, the transmigration of which was enhanced by NMO-IgG (Figure 2). Then, we have shown that blockade of IL-6 signaling in EAE mice suppressed the migration of CD4-positive T cells into the spinal cord, prevented the increase in BBB permeability, and prevented the onset of myelitis (Figures 3 and 4). In addition, NMO-IgG was found to cause significant barrier dysfunction, which was strongest when NMO-IgG was applied to both the vascular and brain parenchymal sides of the model; the effect was not as strong with application of NMO-IgG to the brain parenchymal side, but it was stronger than with vascular application (Figure 5). The application of satralizumab inhibited NMO-IgG–induced barrier dysfunction; application of satralizumab to the vascular and brain parenchymal sides had the highest effect on inhibiting NMO-IgG–induced barrier dysfunction, whereas the effect of applying satralizumab to the brain parenchymal side was almost the same as with vascular application (Figure 5). We also demonstrated that the intracerebral transferability of satralizumab in the presence of NMO-IgG further increased to more than that of NMO-IgG itself (Figure 6).

In earlier studies, we found that autoantibodies to GRP78 in NMO-IgG activate nuclear factor-kappa B (NF-κB) signals in vascular ECs and increase BBB permeability, leading to attack by NMO-IgG on astrocytes on the CNS side of the BBB.[17] We also showed that NMO-IgG on the CNS side induces IL-6 expression in astrocytes and that IL-6 trans-signaling affects ECs and modifies the properties of the BBB, including inducing the expression of several chemokines (CCL2 and CXCL8) and decreasing the expression of claudin-5 as well as increasing the permeability with respect to solutes and increasing the transmigration of PBMCs.[11] In the current study, we demonstrated that brain parenchymal application of NMO-IgG decreased the barrier function more strongly than did vascular application (Figure 4), indicating that the reduction of barrier function by IL-6 signaling on the CNS side is much more than by NMO-IgG on the vascular side.

Therefore, with respect to the pathophysiology of NMOSD at the BBB, there appear to be several steps on both sides of the BBB involved in the onset of NMOSD (Figure 7A). First, NMO-IgG (anti-GRP78 or an unknown antibody or antibodies) activates NF-κB signals in ECs. Second, NMO-IgG decreases the barrier function on the vascular side. Third, NMO-IgG increases the intracerebral transferability of NMO-IgG itself. Fourth, NMO-IgG attacks the AQP4 of astrocytes and induces IL-6 expression in astrocytes. Fifth, IL-6 signaling affects ECs on the CNS side. Sixth, IL-6 signaling more strongly decreases the barrier function on the CNS side than on the vascular side. Seventh, IL-6 signaling induces the expression of several chemokines (CCL2 and CXCL8) in ECs. Eight, the induced chemokines enhance infiltration of inflammatory cells. Finally, NMOSD develops.

To explore the action mechanism of satralizumab at the BBB in NMOSD, we evaluated the intracerebral transferability of satralizumab. Satralizumab was found to have potential intracerebral transferability almost 3 times that of control IgG (Figure 6A), and NMO-IgG was found to have intracerebral transferability almost 1.5 times that of control IgG (Figure 7B). We then found that the intracerebral transferability of satralizumab in the presence of NMO-IgG was significantly increased to almost 3 times that in the presence of control IgG (Figure 6C). These results mean that the intracerebral transferability of satralizumab is enhanced by NMO-IgG and that satralizumab can pass though the BBB and affect the CNS side.

We also demonstrated that satralizumab suppressed the decrease in barrier function induced by NMO-IgG (Figure 5) and prevented NMO-IgG-induced enhancement of inflammatory cell infiltration (Figure 2). In addition, administration of anti-IL-6 receptor antibody to EAE mice prevented T-cell migration and the development of EAE without inhibition of T-cell differentiation (Figure 3). Blockade of IL-6 signaling suppressed the migration of CD4-positive T cells into the spinal cord, prevented the increase in BBB permeability, and prevented the onset of the myelitis in EAE mice. Consequently, with regard to the action mechanism of satralizumab at the BBB in NMOSD, it can be said that satralizumab can pass through the BBB in NMOSD and that blockade of IL-6 from astrocytes on the CNS side suppresses the BBB dysfunction and the induction of inflammatory cell infiltrates, leading to prevention of the onset of NMOSD (Figure 7B). In addition, the finding that satralizumab rescues TEER more significantly when applied to both the vascular and the parenchymal side means that satralizumab might be more effective in acute inflamed sites of NMOSD where NMO-IgG and satralizumab could reach to CNS side due to BBB breakdown.

Because the therapeutic mechanisms of satralizumab at the BBB are as well adapted for action in the acute phase of NMOSD by suppressing leukocyte migration as they are in the recurrence prevention period by inhibiting the barrier dysfunction, treatment with satralizumab is a promising strategy both to reduce the frequency of NMOSD attacks and to treat acute damage. Given the effect of satralizumab on BBB integrity, it may be a new option in the treatment of other conditions such as autoimmune optic neuritis and encephalomyelitis such as neuro-Behcet syndrome, CNS lupus, anti-NMDA receptor encephalitis, and Vogt-Koyanagi-Harada disease,[35-37] all of which induce BBB breakdown and increase IL-6 concentration in the CSF.

As limitations in this study, we did not completely evaluate the off-effect of NMO-IgG and the therapeutic mechanisms of satralizumab at the BBB in vitro experiments. For example, the application of the IgG and satralizumab was simultaneous in the migration assay and the measurement of TEER and intracerebral transferability. Then, in the migration assay, the PBMCs have not been exposed to the satralizumab to evaluate the effect of satralizumab at the only BBB. Further investigations are needed to clarify the effects of satralizumab on both BBB and leukocytes by simultaneous and sequential application of NMO-IgG and satralizumab.

Acknowledgment

The authors thank Yoshihiro Matsumoto and Kenji Yogo of Chugai Pharmaceutical Co., Ltd, for ensuring the integrity of the in vivo study.

Study Funding

This study was supported by research grants from Chugai Pharmaceutical Co., Ltd, and the Japan Society for the Promotion of Science (JSPS) (JP19K07975).

Disclosure

K. Serizawa, H. Tomizawa-Shinohara, and S. Miyake are paid employees of Chugai Pharmaceutical Co., Ltd. Chugai has filed a patent application related to the subject matter of this article (PCT/JP2020/005965; Inhibitory effect of anti-IL-6 receptor antibody on BBB dysfunction). T. Kanda is a member of the advisory board of Chugai Pharmaceutical Co., Ltd. Y. Takeshita and T. Kanda have filed a patent application related to the subject matter of this article (WO2017179375A1, PCT/JP2017/011361; In vitro model for blood-brain barrier and method for producing in vitro model for blood-brain barrier). Go to Neurology.org/NN for full disclosures.

Publication History

Received by *Neurology: Neuroimmunology & Neuroinflammation* January 28, 2021. Accepted in final form June 24, 2021.

Appendix Authors

Name	Location	Contribution
Yukio Takeshita, MD, PhD	Department of Neurology and Clinical Neuroscience, Yamaguchi University Graduate School of Medicine, Yamaguchi, Japan	Drafting/revision of the manuscript for content, including medical writing for content, and major role in the acquisition of data
Susumu Fujikawa, MD	Department of Neurology and Clinical Neuroscience, Yamaguchi University Graduate School of Medicine, Yamaguchi, Japan	Drafting/revision of the manuscript for content, including medical writing for content, and major role in the acquisition of data
Kenichi Serizawa, PhD	Kenichi Serizawa, Haruna Tomizawa-Shinohara and Shota Miyake, Product Research Department, Chugai Pharmaceutical Co., Ltd, Kanagawa, Japan	Drafting/revision of the manuscript for content, including medical writing for content, and analysis or interpretation of data
Miwako Fujisawa, MD	Department of Neurology and Clinical Neuroscience, Yamaguchi University Graduate School of Medicine, Yamaguchi, Japan	Analysis or interpretation of data
Kinya Matsuo, MD	Department of Neurology and Clinical Neuroscience, Yamaguchi University Graduate School of Medicine, Yamaguchi, Japan	Analysis or interpretation of data

Appendix *(continued)*

Name	Location	Contribution
Joe Nemoto, MD	Department of Neurology and Clinical Neuroscience, Yamaguchi University Graduate School of Medicine, Yamaguchi, Japan	Analysis or interpretation of data
Fumitaka Shimizu, MD, PhD	Department of Neurology and Clinical Neuroscience, Yamaguchi University Graduate School of Medicine, Yamaguchi, Japan	Analysis or interpretation of data
Yasuteru Sano, MD, PhD	Department of Neurology and Clinical Neuroscience, Yamaguchi University Graduate School of Medicine, Yamaguchi, Japan	Analysis or interpretation of data
Haruna Tomizawa-Shinohara, PhD	Kenichi Serizawa, Haruna Tomizawa-Shinohara and Shota Miyake, Product Research Department, Chugai Pharmaceutical Co., Ltd, Kanagawa, Japan	Analysis or interpretation of data
Shota Miyake	Kenichi Serizawa, Haruna Tomizawa-Shinohara and Shota Miyake, Product Research Department, Chugai Pharmaceutical Co., Ltd, Kanagawa, Japan	Analysis or interpretation of data
Richard M. Ransohoff, MD, PhD	Richard M Ransohoff, Third Rock Ventures, Boston	Study concept or design
Takashi Kanda, MD, PhD	Department of Neurology and Clinical Neuroscience, Yamaguchi University Graduate School of Medicine, Yamaguchi, Japan	Study concept or design

References

1. Jacob A, McKeon A, Nakashima I, et al. Current concept of neuromyelitis optica (NMO) and NMO spectrum disorders. *J Neurol Neurosurg Psychiatry*. 2013;84(8):922-930.
2. Wingerchuk DM, Banwell B, Bennett JL, et al., International Panel for NMO Diagnosis, International consensus diagnostic criteria for neuromyelitis optica spectrum disorders. *Neurology*. 2015;85(2):177-189.
3. Lennon VA, Wingerchuk DM, Kryzer TJ, et al. A serum autoantibody marker of neuromyelitis optica: distinction from multiple sclerosis. *Lancet*. 2004;364(9451):2106-2112.
4. Lennon VA, Kryzer TJ, Pittock SJ, Verkman AS, Hinson SR. IgG marker of optic-spinal multiple sclerosis bind to the aquaporin-4 water channel. *J Exp Med*. 2005;202(4):473-477.
5. Saadoun S, Waters P, Bell BA, Vincent A, Verkman AS, Papadopoulos MC. Intracerebral injection of neuromyelitis optica immunoglobulin G and human complement produces neuromyelitis optica lesions in mice. *Brain*. 2010;133(Pt 2):349-361.
6. Zhang H, Bennett JL, Verkman AS. Ex vivo spinal cord slice model of neuromyelitis optica reveals novel immunopathogenic mechanisms. *Ann Neurol*. 2011;70(6):943-954.
7. Papadopoulos MC, Verkman AS. Aquaporin 4 and neuromyelitis optica. *Lancet Neurol*. 2012;11(6):535-544.
8. Majed M, Fryer JP, McKeon A, Lennon VA, Pittock SJ. Clinical utility of testing AQP4-IgG in CSF: guidance for physicians. *Neurol Neuroimmunol Neuroinflamm*. 2016;3(3):e231.
9. Shimizu F, Sano Y, Takahashi T, et al. Sera from neuromyelitis optica patients disrupt the blood-brain barrier. *J Neurol Neurosurg Psychiatry*. 2012;83(3):288-297.
10. Obermeier B, Daneman R, Ransohoff RM. Development, maintenance and disruption of the blood-brain barrier. *Nat Med*. 2013;19(12):1584-1596.
11. Takeshita Y, Obermeier B, Cotleur AC, et al. Effects of neuromyelitis optica-IgG at the blood-brain barrier in vitro. *Neurol Neuroimmunol Neuroinflamm*. 2016;4(1):e311.
12. Hosokawa T, Nakajima H, Doi Y, et al. Increased serum matrix metalloproteinase-9 in neuromyelitis optica: implication of disruption of blood-brain barrier. *J Neuroimmunol*. 2011;236(1-2):81-86.
13. Tomizawa Y, Yokoyama K, Saiki S, Takahashi T, Matsuoka J, Hattori N. Blood-brain barrier disruption is more severe in neuromyelitis optica than in multiple sclerosis and correlates with clinical disability. *J Int Med Res*. 2012;40(4):1483-91.
14. Matsushita T, Tateishi T, Isobe N, et al. Characteristic cerebrospinal fluid cytokine/chemokine profiles in neuromyelitis optica, relapsing remitting or primary progressive multiple sclerosis. *Plos One*. 2013;8(4):e61835.
15. Uzawa A, Mori M, Ito M, et al. Markedly increased CSF interleukin-6 levels in neuromyelitis optica, but not in multiple sclerosis. *J Neurol*. 2009;256(12):2082-2084.
16. Uzawa A, Mori M, Arai K, et al. Cytokine and chemokine profiles in neuromyelitis optica: significance of interleukin-6. *Mult Scler*. 2010;16(12):1443-1452.
17. Chihara N, Aranami T, Sato W, et al. Interleukin 6 signaling promotes anti-aquaporin 4 autoantibody production from plasmablasts in neuromyelitis optica. *Proc Natl Acad Sci USA*. 2011;108(9):3701-3706.
18. Shimizu F, Schaller KL, Owens GP, et al. Glucose-regulated protein 78 autoantibody associates with blood-brain barrier disruption in neuromyelitis optica. *Sci Transl Med*. 2017;9(397):eaai9111.
19. Rochfort KD, Collins LE, Murphy RP, Cummins PM. Downregulation of blood-brain barrier phenotype by proinflammatory cytokines involves NADPH oxidase-dependent ROS generation: consequences for interendothelial adherens and tight junctions. *Plos One*. 2014;9(7):e101815.
20. Uchida T, Mori M, Uzawa A, et al. Increased cerebrospinal fluid metalloproteinase-2 and interleukin-6 are associated with albumin quotient in neuromyelitis optica: their possible role on blood-brain barrier disruption. *Mult Scler*. 2017;23(8):1072-1084.
21. Araki M, Matsuoka T, Miyamoto K, et al. Efficacy of the anti-IL-6 receptor antibody tocilizumab in neuromyelitis optica: a pilot study. *Neurology*. 2014;82(15):1302-1306.
22. Ayzenberg I, Kleiter I, Schröder A, et al. Interleukin 6 receptor blockade in patients with neuromyelitis optica nonresponsive to anti-CD20 therapy. *JAMA Neurol*. 2013;70(3):394-397.
23. Reichert JM. Antibodies to watch in 2017. *MAbs*. 2017;9(2):167-181.
24. Igawa T, Ishii S, Tachibana T, et al. Antibody recycling by engineered pH-dependent antigen binding improves the duration of antigen neutralization. *Nat Biotechnol*. 2010;28(11):1203-1207.
25. Igawa T, Tsunoda H, Tachibana T, et al. Reduced elimination of IgG antibodies by engineering the variable region. *Protein Eng Des Sel*. 2010;23(5):385-392.
26. Yamamura T, Kleiter I, Fujihara K, et al. Trial of satralizumab in neuromyelitis optica spectrum disorder. *N Engl J Med*. 2019;381(22):2114-2124.
27. Takeshita Y, Ransohoff RM. Inflammatory cell trafficking across the blood-brain barrier: chemokine regulation and in vitro models. *Immunol Rev*. 2012;248(1):228-239.
28. Sano Y, Shimizu F, Abe M, et al. Establishment of a new conditionally immortalized human brain microvascular endothelial cell line retaining an in vivo blood–brain barrier function. *J Cell Physiol*. 2010;225(2):519-528.
29. Shimizu F, Sano Y, Tominaga O, Maeda T, Abe MA, Kanda T. Advanced glycation end-products disrupt the blood-brain barrier by stimulating the release of transforming growth factor-β by pericytes and vascular endothelial growth factor and matrix metalloproteinase-2 by endothelial cells in vitro. *Neurobiol Aging*. 2013;34(7):1902-1912.
30. Takeshita Y, Obermeier B, Cotleur A, Sano Y, Kanda T, Ransohoff RM. An in vitro blood-brain barrier model combining shear stress and endothelial cell/astrocyte co-culture. *J Neurosci Methods*. 2014;232:165-172.
31. Man S, Tucky B, Cotleur A, Drazba J, Takeshita Y, Ransohoff RM. CXCL12-induced monocyte-endothelial interactions promote lymphocyte transmigration across an in vitro blood-brain barrier. *Sci Transl Med*. 2012;4(119):119ra14.
32. Serizawa K, Tomizawa-Shinohara H, Magi M, Yogo K, Matsumoto Y. Anti-IL-6 receptor antibody improves pain symptoms in mice with experimental autoimmune encephalomyelitis. *J Neuroimmunol*. 2018;319(682):71-79.
33. Haruki H, Sano Y, Shimizu F, et al. NMO sera down-regulate AQP4 in human astrocyte and induce cytotoxicity independent of complement. *J Neurol Sci*. 2013;331(1-2):136-144.
34. Shimizu F, Sano Y, Maeda T, et al. Peripheral nerve pericytes originating from the blood-nerve barrier expresses tight junctional molecules and transporters as barrier-forming cells. *J Cell Physiol*. 2008;217(2):388-399.
35. Lin P. Targeting interleukin-6 for noninfectious uveitis. *Clin Ophthalmol*. 2015;9:1697-1702.
36. Yoshimura T, Sonoda KH, Ohguro N, et al. Involvement of Th17 cells and the effect of anti-IL-6 therapy in autoimmune uveitis. *Rheumatology*. 2009;48(4):347-354.
37. Asano T, Ito H, Kariya Y, et al. Evaluation of blood-brain barrier function by quotient alpha2 macroglobulin and its relationship with interleukin-6 and complement component 3 levels in neuropsychiatric systemic lupus. *Plos One*. 2017;12(10):e0186414.
38. Okazaki M, Yamada Y, Nishimoto N, Yoshizaki K, Mihara M. Characterization of anti-mouse interleukin-6 receptor antibody. *Immunol Lett*. 2002;84(3):231-240.